Sampling Rules for an Inhomogeneous Plane-Wave Representation of Scattered Fields

Quentin Gueuning, Christophe Craeye, *Senior Member, IEEE*, and Claude Oestges, *Fellow, IEEE*

***Abstract*— Inhomogeneous plane waves (IPWs) based on a linear contour deformation provide an accurate and concise field representation for scattering problems in which source and observation domains are visible within a limited angular sector. Given an error level, we derive closed-form expressions for the truncation limit, the sampling step, and the contour slope that minimize the number of plane waves. A relation is drawn between the required number of plane waves and the degrees of freedom of the field, defined as the minimum number of orthonormal basis functions that represents scattered fields. The sampling rules are then applied to an efficient evaluation of the physical optics radiation integral.**

***Index Terms*— Computational electromagnetics, contour deformation, degrees of freedom (DoF), error analysis, fast algorithm, field representation, Green's function, inhomogeneous plane waves (IPWs), physical optics (PO), scattering, spectral-domain method.**

I. Introduction

OVER the past years, inhomogeneous plane-wave (IPW) methods have been developed to accelerate full-wave simulations of radar cross sections, input impedances, radiation patterns of both electrically large and small objects [1], [2], which can possibly lie above or below a penetrable ground [3]–[5] and physical optics (PO) simulations of the radio-coverage of base station antennas located in urban environments [6], in which facets with a size of hundreds wavelengths stand in each other near fields.

Since the emergence of fast computational methods for high-frequency electromagnetics in the 1980s, many field representations have been successfully proposed and applied, e.g., the multipole decomposition [7], the spherical wave functions [8], the Slepian's prolate spheroidal wave functions [9], [10], the complex point source [11], the homogeneous [12], and the IPWs [13]. In one way or another, they all exploit the quasi band limitation of the scattered fields outside the reactive region [14]. Consequently, an efficient field reconstruction is achieved when the required number of coefficients is as close as possible to the degrees of freedom (DoF) [15] for a given accuracy. Nowadays, a remaining challenge concerns the mathematical derivation of invertible error models. For arbitrary geometries, such models form the only way to guarantee the accuracy of accelerated methods.

The IPW decomposition originates from a spectral representation of the fields in a given reference plane, each Fourier component corresponding to a plane wave. Then, a contour deformation is applied to circumvent the singularities and accelerate the numerical convergence. Because of the complex-valued wavevectors, the plane waves, qualified as "inhomogeneous," are both propagating and evanescent in the direction orthogonal to the reference plane. This expansion is particularly well suited to scattering problems in which source and observation domains see each other through a sufficiently small angular sector. Indeed, as will be demonstrated later, the required number of plane waves is proportional to the electrical dimensions of the scatterer and to the size of the observation sector. The IPW decomposition was exploited by Michielssen and Chew [13] in the computational electromagnetics area to develop a fast integral-equation solver. The selected contour was the steepest descent path (SDP) in the angular domain since it annihilates the oscillations of the integrand around a given saddle point [16]. It is then possible to keep only the plane waves for which the wavevectors have a limited real part. Later in [1], the SDP was found impractical for large groups due to the presence of peaks and oscillations in the integrand. Hence, it is distorted into a discontinuous path including an interval on the real axis. The method, called fast inhomogeneous plane-wave algorithm (FIPWA), is less sensitive to numerical instabilities than the fast multipole method (FMM) [7]. An important issue concerns the discretization of the translation function in FIPWA for a fixed error level according to the electrical size of the boxes and the relative distance between them. A strategy for the control of the truncation and extrapolation errors is presented in [17]. However, no general rules for error control are available so far. Among the many fast methods, FIPWA has shown the ability to accurately reconstruct the reactive fields [2], [3] in which the evanescent waves prevail. The IPW decompositions also inherit a long history of field analysis in multilayered media [4], [18]–[20]. Recently, thanks to a change of the integration variables from angles to wavevectors [21], it was demonstrated in [22] and [23] that the integration with rectangles is efficient since the integrand

Manuscript received September 4, 2017; revised September 28, 2018; accepted October 8, 2018. Date of publication December 6, 2018; date of current version March 5, 2019. This work was supported in part by the WB-Health Program of Walloon Region through the Research Project B-WARE, in part by the BESTCOM Interuniversity Belgian Research Program, and in part by F.R.S.-FNRS through the Research Project MACHAON. *(Corresponding author: Quentin Gueuning.)*

The authors are with the Institute of Information and Communication Technologies, Electronics and Applied Mathematics, Université catholique de Louvain, 1348 Louvain-la-Neuve, Belgium (e-mail: quentin.gueuning@uclouvain.be; christophe.craeye@uclouvain.be; claude.oestges@uclouvain.be).

Digital Object Identifier 10.1109/TAP.2018.2885414

along the SDP resembles the Fourier transform of a modulated Gaussian function when the field is evaluated inside a small angular sector. In addition, an integration scheme that benefits from a compensation between the aliasing and the truncation errors has been developed.

In this paper, we analyze the numerical errors inherent to an IPW field decomposition with a parameterized linear contour. The analysis is carried out on the scalar free-space Green's function under the paraxial approximation and does not directly rely on the concept of quasi band limitation. First, the truncation error as a result of the spectral domain finiteness, the discretization error as a result of the integrand sampling, and the rounding error as a result of the computer's finite precision are derived, discussed, and inverted in order to provide concise expressions and validity conditions for the truncation limit, the sampling step, and the contour slope. Afterward, we will estimate the number of plane waves and the contour slope that minimizes it. A relation with the DoF of fields is also carried out. This is an improvement compared to [22] where error models developed for an SDP contour were not inverted and the number of required plane waves was tabulated. Finally, the sampling rules are validated through the evaluation of the near-field PO radiation integral from a planar surface. Making use of Green's theorem ([6], [24], [25] and Appendix B), the resulting formulation extends the spectral integration proposed in [26] to complex-wavenumber spectra. Hence, the spectral integration is no longer subject to numerical instabilities owing to the free-space critical pole and the computation method does not require any spatial mesh.

The remainder of this paper is organized as follows. Section II recalls the plane-wave decomposition for scattered fields. In Section III, mathematical models for truncation, discretization, and round-off errors are developed and inverted, making use of a paraxial approximation. In Section IV, we estimate the number of plane waves required for a given relative error and evaluate the contour slope that minimizes it. Then, the sampling rules are applied to the PO evaluation of the field scattered by a planar surface in Section V. Finally, perspectives and conclusions are drawn in Section VI.

II. Spectral-Domain Formulation

Considering an observation point $\mathbf{r} = x\hat{\mathbf{x}} + y\hat{\mathbf{y}} + z\hat{\mathbf{z}}$ with $z \geq 0$ and a radial distance $\rho = (x^2 + y^2)^{1/2}$, the spectral decomposition of the 3-D free-space scalar Green's function, respectively, in cylindrical and Cartesian coordinates, is [27]

$$G(r) = \frac{e^{-jkr}}{4\pi r} = \frac{-j}{4\pi}\int_0^\infty \frac{e^{-jk_z|z|}}{k_z} J_0(k_\rho \rho) k_\rho \frac{\mathrm{d}k_\rho}{\mathrm{d}k_{\rho r}} \mathrm{d}k_{\rho r} \quad (1)$$

$$= \frac{-j}{8\pi^2}\iint_{-\infty}^{\infty} \frac{e^{-j\mathbf{k}\cdot\mathbf{r}}}{k_z} \frac{k_\rho}{k_{\rho r}} \frac{\mathrm{d}k_\rho}{\mathrm{d}k_{\rho r}} \mathrm{d}k_{xr}\mathrm{d}k_{yr} \quad (2)$$

where k is the free-space wavenumber, J_0 is the first-order Bessel function of the first kind, $\mathbf{k} = k_x\hat{x} + k_y\hat{y} + k_z\hat{z}$ is the complex spectral wavevector, and the radial component $k_\rho = (k_x + k_y)^{1/2}$ follows a path in the complex plane to circumvent the free-space branch point at $k_\rho = k$ and to accelerate the numerical convergence. The function $\mathrm{d}k_\rho/\mathrm{d}k_{\rho r} = (1 + j\mathrm{d}k_{\rho i}/\mathrm{d}k_{\rho r})$ results from the contour integration and the fraction $k_\rho/k_{\rho r}$ stems from a polar-to-cartesian change of variables [21].

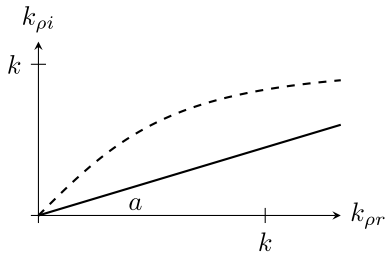

Fig. 1. Two unclosed contours: the SDP (dashed) and linear contour (straight).

The shape of the contour and its parametrization are entirely governed by the critical dimensions of the source and the observation domain, i.e., the distance z/λ and the field of view ρ/z, as well as by the targeted relative error ϵ. For example, when the distance z is much larger than the wavelength and the field of view is much smaller than one, the SDP, shown in Fig. 1, is relevant because it keeps the imaginary part of the exponent $-jk_{zi}$ constant. However, when the field of view increases, the integrand starts to oscillate and its amplitude grows considerably. Consequently, its numerical integration along the SDP is no longer optimal and, in some cases, not even converging. In order to derive concise relations for the error models, we will only consider a linear contour of slope a virtually closed at $k_{\rho r} = \infty$, as sketched in Fig. 1.

In the spatial domain, the scattered electric field is obtained as a convolution of the induced surface electric currents $\mathbf{J}$ on the source domain S' with Green's function [30]

$$\mathbf{E}^s(\mathbf{r}) = -jk\eta \iint \mathbf{G}(\mathbf{r}, \mathbf{r}') \cdot \mathbf{J}(\mathbf{r}')\mathrm{d}S' \quad (3)$$

where η is the free-space impedance, $\mathbf{r}'$ is the position of a source point, $\mathbf{G} = (1 + 1/k^2\nabla\nabla\cdot)G(r)\mathbf{I}$ is the electric dyadic Green's function, $\mathbf{I}$ is the identity matrix, and $\nabla\nabla\cdot$ is the grad-div operator. Inserting the discretized form of (2) into (3) and swapping sums and integrals leads to a spectral-domain formulation [3]

$$\mathbf{E}^d(\mathbf{r}) = \sum_p \sum_q w_{pq} \tilde{\mathbf{E}}^s(\mathbf{k}_{pq}) e^{-jk_{x,pq}x} e^{-jk_{y,pq}y} e^{-jk_{z,pq}z} \quad (4)$$

where the superscript d stands for discrete representation and the spectral weight is

$$w_{pq} = \frac{-j\Delta k^2}{8\pi^2} \frac{1}{k_{z,pq}} \frac{k_{\rho,pq}}{k_{\rho r,pq}} \frac{\mathrm{d}k_{\rho,pq}}{\mathrm{d}k_{\rho r,pq}} \quad (5)$$

with Δk, the sampling step along real spectral coordinates. The plane-wave spectrum (PWS) of the scattered field, sometimes called the complex pattern, is expressed as

$$\tilde{\mathbf{E}}^s(\mathbf{k}) = -jk\eta \left(\tilde{\mathbf{J}}(\mathbf{k}) - (\tilde{\mathbf{J}}(\mathbf{k}) \cdot \mathbf{k})\mathbf{k}/k^2\right) \quad (6)$$

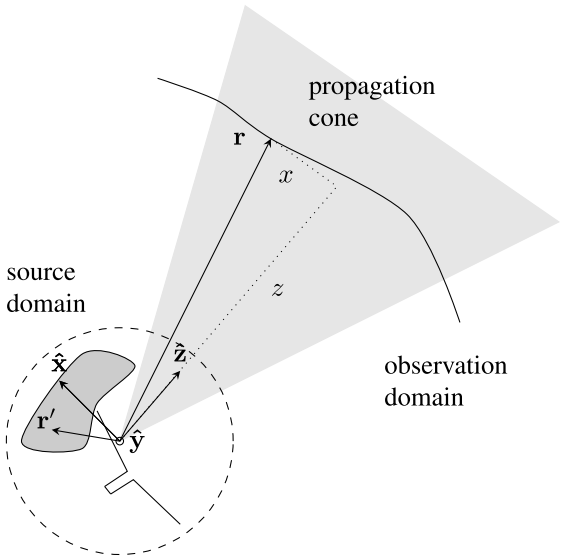

Fig. 2. Cut view of the problem geometry with a local CS.

where the PWS of the current distribution is given by

$$\tilde{\mathbf{J}}(\mathbf{k}) = \iint \mathbf{J}(\mathbf{r}')e^{j\mathbf{k}\cdot\mathbf{r}'}\mathrm{d}S'. \tag{7}$$

The integrals (4) and (7) must be evaluated in a local system of coordinates (CS) with $(\hat{\mathbf{x}}, \hat{\mathbf{y}}, \hat{\mathbf{z}})$ centered on the scatterer domain and oriented toward the observation domain, as shown in Fig. 2. This results from the dependence of the contour deformation on the direction of the z-axis.

Given that the coordinates k_{zpq} have real and imaginary parts, the plane waves, qualified as "inhomogeneous," are both propagating and evanescent with respect to the forward direction $\hat{\mathbf{z}}$. A property of any plane-wave expansion is the separability of the source and observation coordinates within the spectral integral (2). From a computational perspective, this separability allows us to store the samples of the PWS (6) and reuse them for another field evaluation. From a physical perspective, the plane waves, which are solutions to Maxwell's equations, can further propagate and provide a field representation over an extended domain. In contrast to purely propagating plane-wave expansions, e.g., in the FMM algorithm, the inhomogeneous plane-wave decomposition is spatially selective. Indeed, the field can only be reconstructed inside a conical region, as depicted in Fig. 2. As we will see in Section IV, the number of plane waves required in (4) to achieve a given accuracy ϵ is proportional to the square of electrical dimensions of the domains ρ/λ and to the square of the field of view ρ/z. Moreover, the IPW field expansion is not exposed to numerical instabilities when the observation point approaches the source since it does not entail the attempt to extract near-field information from far-field patterns.

III. Numerical Errors

In this section, the mathematical identities are established for the estimation of error sources inherent to the numerical integration in (2), i.e., the truncation error as a result of the spectral domain finiteness, the discretization error as a result of the integrand sampling, and the rounding error as a result of the computer's finite precision.

In the following mathematical derivations, we will repetitively use a paraxial, or small-angle, an approximation. In the spectral domain, it consists of replacing $k_z \approx k$ in the denominator [22] and of performing a second order Taylor's series of k_z in the exponential

$$k_z \approx k - \frac{k_\rho^2}{2k} \tag{8}$$

which is accurate when $|k_m| \ll k$. After substituting those approximations in the plane-wave decomposition of Green's function, (2) becomes the 2-D Fourier transform of a Gaussian function which is equal to

$$G(r) \approx \frac{e^{-jkz-jk\rho^2/(2z)}}{4\pi z}. \tag{9}$$

Clearly, this relation establishes an equivalence with the paraxial approximation of Green's function in the spatial domain which requires $\rho \ll z$ and $kz \gg 1$, i.e., a field of view much smaller than one and a distance z much larger than the wavelength. Moreover, additional conditions on the contour slope a will be introduced subject to the errors resulting from the numerical integration of the exact integrand and the integrand approximated with (8) are comparable. In addition, we will make use of the near-field coefficient defined in [28] as

$$C = 2\pi F = \frac{k\rho^2}{z} = \frac{\pi}{4}\frac{z_f}{z} \tag{10}$$

where F is the Fresnel number and $z_f = 8\rho^2/\lambda$ is the Fraunhoffer limit. $C \ll 1$ corresponds to the far-field region and $C \gg 1$ corresponds to the intermediate-to-near-field region. It is important to mention that the paraxial approximations will be limited to the determination of the sampling rules, while the exact formulation will be used for field calculations. It will be shown in Section V that the error models derived in that way can still be used to represent the field in the intermediate-to-near-field region.

In this paragraph, we explain why the error levels derived for the scalar Green's function can be extended to vector fields. As demonstrated in [14], the absolute error resulting from a field decomposition is bounded by the product of the maximum possible field value and an error measure of the dyadic Green's function

$$|\mathbf{E}^d(\mathbf{r}) - \mathbf{E}^s(\mathbf{r})| \leq |\mathbf{E}^{\max}| \cdot |\bar{\boldsymbol{\epsilon}}| \tag{11}$$

with

$$|\mathbf{E}^{\max}| = \frac{-jk\eta}{d_{\min}} \iint |\mathbf{J}(\mathbf{r}')| dS'$$
$$|\bar{\boldsymbol{\epsilon}}| = d_{\min} \max_{\mathbf{r},\mathbf{r}'} |\bar{\mathbf{G}}^d(\mathbf{r},\mathbf{r}') - \bar{\mathbf{G}}(\mathbf{r},\mathbf{r}')|$$

where $\bar{\boldsymbol{\epsilon}}$ is a matrix and $d_{\min}$ is the minimum distance between the source and observation domains. The upper bound (11) links the maximum absolute error of the electrical field with that of the dyadic Green's function. This relation is no longer valid for the relative error. Indeed, the field can be much lower than its maximum value within some observation domains, e.g., in the shadow region of a scatterer or around the sidelobes

of a directive antenna. This issue will be highlighted through an example in Section V.

It is proven in Appendix C that the elements of $\bar{\epsilon}$ are of the same order of magnitude as the relative error of the scalar Green's function G

$$\epsilon = \frac{G(r) - G^d(r)}{G(r)} \tag{12}$$

where G^d is the discrete IPW decomposition of G. In the following, we will, thus, only analyze ϵ.

A. Truncation Error

The $k_x k_y$ spectral domain is limited to a disk of radius k_{mr}. Compared to a square integration domain, the area is reduced by a factor $\pi/4$ and the error ϵ is axially symmetrical. The corresponding complex-valued limit is given by $k_m = k_{mr} + jk_{mi}$.

When the approximation (8) holds, the truncation error can be estimated with the help of (1), (8), and (9) as

$$\epsilon \approx \frac{-jz}{k} e^{jk\rho^2/(2z)} \int_{k_m}^{\infty} e^{jk_\rho^2 z/(2k)} J_0(k_\rho \rho) k_\rho \mathrm{d}k_\rho. \tag{13}$$

Then, as proven in Appendix A, the error can be approximately bounded by

$$-\ln|\epsilon| \gtrsim k_{mr} k_{mi} z/k - k_{mi}\rho. \tag{14}$$

From there, for a linear contour deformation of slope a, i.e., for $k_{mi} = ak_{mr}$, the truncation limit is given by the root of a quadratic polynomial

$$k_{mr} \gtrsim \frac{k\rho}{z}\left(\frac{1}{2} + \sqrt{\frac{1}{4} - \frac{\ln|\epsilon|}{aC}}\right). \tag{15}$$

The spectral approximation (8) made in (13) requires $|k_m| \ll k$. By considering successively the real and the imaginary parts of k_m, we can extract four underlying conditions given (15)

$$\frac{\rho}{z} \ll 1, \quad a \ll \frac{z}{\rho}, \quad a \ll \frac{-kz}{\ln|\epsilon|}, \quad a \gg \frac{-\ln|\epsilon|}{kz}. \tag{16}$$

The first condition defines the paraxial regime. The second condition will always be satisfied since the optimal contour slope is smaller than one, as shown later. The third and fourth conditions generate an interval for the contour slope which is not restrictive when the distance z is much larger than the wavelength.

In Fig. 3, the upper bound (14) is validated for three values of the linear contour slope a and distances z selected to satisfy (16). The large range of validity of (14) is observed. One can see that the solid curve (upper bound) is always above to the dashed curve (exact error). The stabilization of the exact error around 10^{-14} at the lower values of ρ/λ can most likely be associated with the round-off error.

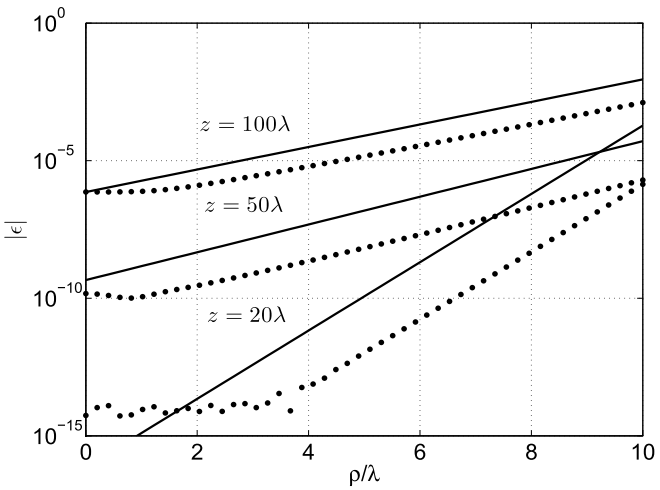

Fig. 3. Upper bound (solid) and exact value (dotted) of the truncation error for $a = \{0.7, 0.5, 1\}$, $z = \{20, 50, 100\}\lambda$, $k_{mr} = \{0.7, 0.37, 0.15\}k$.

B. Discretization Error

We will now consider a numerical integration performed in the $k_x k_y$ spectral domain with a rectangle rule using a left endpoint approximation of the integrand. Discretizing (1) with a rate Δk is equivalent to multiplying the integrand with the Fourier series of a Dirac comb

$$\epsilon = \frac{-j}{8\pi^2\, G(r)} \iint \frac{e^{-j\mathbf{k}\cdot\mathbf{r}}}{k_z} \frac{k_\rho}{k_{\rho r}} \frac{\mathrm{d}k_\rho}{\mathrm{d}k_{\rho r}} \times \sum_m \sum_n e^{-jk_{xr} 2\pi m/\Delta k - jk_{yr} 2\pi n/\Delta k} \mathrm{d}k_{xr} \mathrm{d}k_{yr} \tag{17}$$

where $(n, m) \in \mathbb{Z}_0^2$ and the term $(0, 0)$ corresponds to the exact plane-wave decomposition of Green's function (2). After swapping sums and integrals and grouping the arguments of the exponentials, we can identify for each term a complex modulation factor in the spectral domain corresponding to a complex-valued shift in the spatial domain [6]

$$\epsilon = \frac{1}{G(r)} \sum_m \sum_n G\left(r_{mn}\right) \tag{18}$$

where the complex-valued distance is

$$r_{mn} = \left((x - m\Delta x)^2 + (y - n\Delta y)^2 + z^2\right)^{1/2} \tag{19}$$

and $\Delta y = \Delta x = 2\pi/(\Delta k(1 + ja))$ are complex shifts in the spatial domain. For the case $|\Delta y| \ll z$ and an observation domain within a disk of radius ρ, it is proven in Appendix B that the error is

$$-\ln|\epsilon| \approx \frac{2\pi ka}{z\Delta k(1 + a^2)} \left(\frac{2\pi}{\Delta k(1 + a^2)} - \rho\right). \tag{20}$$

The inverse relation for the sampling step Δk is again obtained through the root of a quadratic polynomial

$$\Delta k = \frac{2\pi}{(1 + a^2)\rho} \left(\frac{1}{2} + \sqrt{\frac{1}{4} - \frac{\ln|\epsilon|}{aC}}\right)^{-1}. \tag{21}$$

Expression (21) is accurate when $|\Delta y| \ll z$ and it can be proven that the underlying conditions are exactly those of (16).

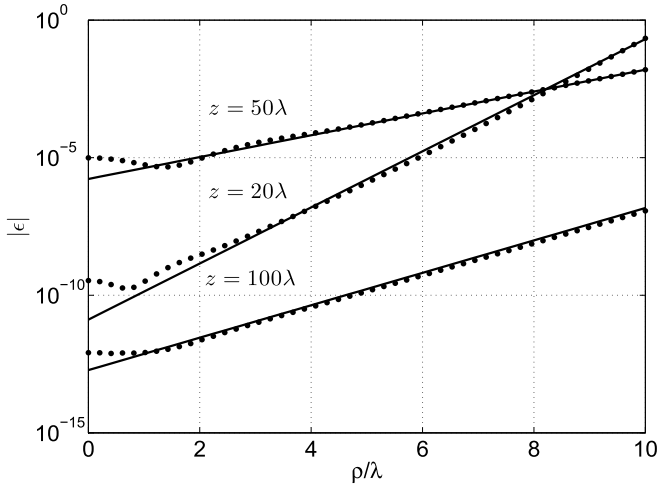

Fig. 4. Model (solid) and exact value (dotted) of the discretization error for $a = \{0.7, 0.5, 1\}$, $z = \{20, 50, 100\}\lambda$, $dk = \{63, 55, 23\}10^{-3}k$.

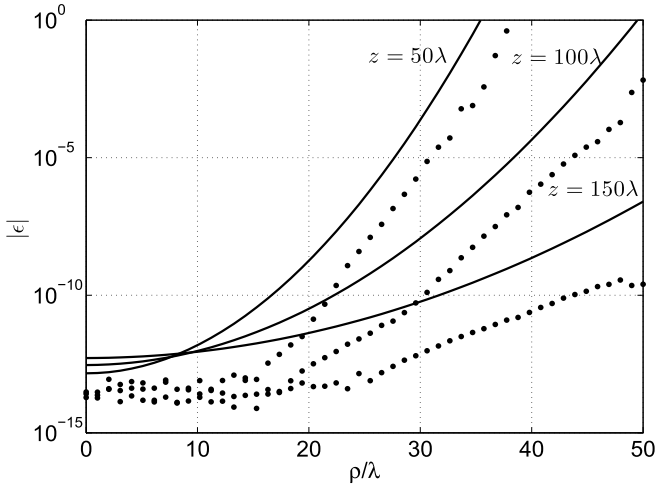

Fig. 5. Upper bound (solid) and exact value (dotted) of the round-off error for $a = \{0.75, 0.75, 0.5\}$, $z = \{50, 100, 150\}\lambda$.

The identity (18) can be interpreted as a generalization of the Nyquist–Shannon sampling theorem to Laplace transforms on a linear path and takes implicitly into account the intricacy of contouring the free-space singularity. It also establishes an equivalence between a discrete plane-wave representation and an infinite set of parasitic sources with complex-valued translated coordinates. The model of (20) is validated in Fig. 4 for the same contour slopes and distances as in Fig. 3. One can observe that the numerically computed relative error ϵ (dotted) is almost superimposed with the model (solid). For lower values of ρ/λ, we note a little discrepancy associated with the contribution of the three other nearest replicas in (18).

C. Round-Off Error

When the electrical dimensions ρ/λ increase, the integrand of (2) quickly grows by several orders of magnitude while Green's function does not. Indeed, the integrand samples oscillate and should, thus, compensate each other. However, owing to the finite precision with which calculations are carried out, a round-off error remains. This ill-conditioning is inherent to any inhomogeneous plane-wave decomposition since its basis element, the IPW, is growing exponentially with respect to xy due to the presence of the $e^{k_{xi}x+k_{yi}y}$ factor in the spectral integral (2).

Considering a random complex-valued noise $n(k_{xr}, k_{yr})$ and the approximation (8), it is proven in Appendix D that the relative round-off error can be approximated by

$$\epsilon \approx \frac{-jz^2}{2\pi} e^{jk\rho^2/(2z)} \iint n e^{jk_\rho^2 z/(2k)} e^{-jk_x x - jk_y y} \frac{k_\rho}{k_{\rho r}} \frac{\mathrm{d}k_\rho}{\mathrm{d}k_{\rho r}} \mathrm{d}k_{xr} \mathrm{d}k_{yr}. \quad (22)$$

As also proven in Appendix D, it can be bounded by

$$|\epsilon| \leq kz\epsilon_m \frac{1+a^2}{a} e^{ak\rho^2/(4z)} \quad (23)$$

where $\epsilon_m = 2.2\ 10^{-16}$ corresponds to the machine error level for double precision. Noticing that $e^x/x \leq e^x$ when $x > 1$ and that the approximation $1 + a^2 \approx 1$ holds since the optimal contour slope is always less than 1 (see in Section IV), the inverse relation provides a maximum value for the contour slope

$$a \leq \frac{4}{C} \ln\left(\frac{|\epsilon|}{\epsilon_m (k\rho)^2}\right) \quad (24)$$

when $4\epsilon/(\epsilon_m(k\rho)^2) > 1$. This inequality implies that the contour slope should be lowered when the near-field coefficient increases. The exact round-off error and its upper bound (23) are compared in Fig. 5 for three distances and contour slopes selected subject to the distances is in the order of dozens of wavelength and the round-off error starts to affect the numerical integration.

IV. Optimal Integration Scheme

In this section, we evaluate the number of plane waves P required to achieve a given relative error ϵ. For the 2-D plane-wave representation of (2), it is approximately given by

$$P \approx \pi \left(\frac{k_{mr}}{\Delta k}\right)^2 \quad (25)$$

where the factor π results from the integration over a disk. In practice, P is obtained by solving a Gauss circle problem [31] and can slightly differ from approximation (25). Targeting equal truncation and discretization errors, it is demonstrated in Appendix E with the help of (15), (21), and (25) that

$$\sqrt{\pi P} \sim \frac{C}{2}(1+a^2)\left(1 - \frac{2\ln|\epsilon|}{aC}\right) \quad (26)$$

where we assume that the overestimation of P resulting from the use of the lower bound (15) is small because of the slow dependence of k_{mr} with respect to ϵ. The contour slope that minimizes P is obtained by cancelling out the derivatives of (26) and solving the following cubic equation:

$$-\frac{C}{\ln|\epsilon|}a^3 + a^2 - 1 = 0 \quad (27)$$

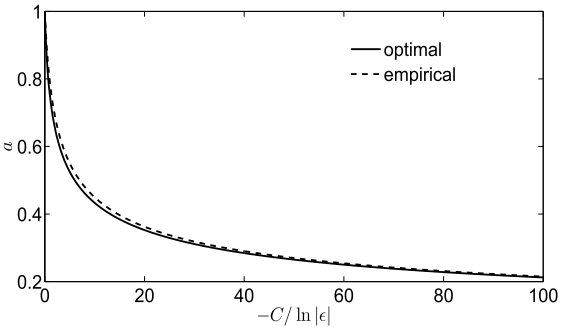

Fig. 6. Optimal and empirical contour slope a as function of $-C/\ln|\epsilon|$.

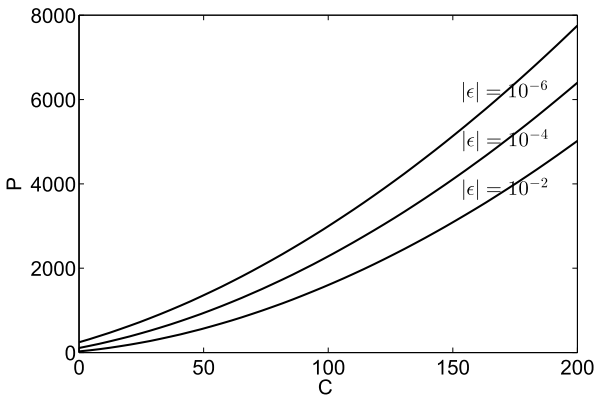

Fig. 7. Required number of plane waves versus the near-field parameter C for three relative errors.

for which the real positive root is developed in Appendix F. Since the expression (63) is relatively heavy, we will analyze its asymptotic behavior. When the coefficient $-C/\ln|\epsilon|$ is much larger than 1 (e.g., in the near field and/or for low accuracy), the second-order term of (27) becomes negligible compared to the third order. Then, solving the reduced cubic equation yields

$$a \sim \left(\frac{-\ln|\epsilon|}{C}\right)^{1/3}. \tag{28}$$

When the coefficient $-C/\ln|\epsilon|$ is much smaller than 1 (e.g., in the far field and/or for high accuracy), we can neglect the third-order term of (27) and obtain

$$a \approx 1. \tag{29}$$

Instead of the relatively heavy expression (63) given in Appendix F, the user may consider (28) and (29), combined with an empirical transition rule, such as

$$a = \left(1 - \frac{C}{\ln|\epsilon|}\right)^{-1/3}. \tag{30}$$

From Fig. 6, one can infer that the empirical slope of (30) agrees well with the optimal slope of (63).

For the case where the asymptotic expression (28) is accurate, i.e., $-C/\ln|\epsilon| \gg 1$, it is proven in Appendix E that the number of plane waves is asymptotically given by

$$P \sim \frac{C^2}{4\pi}\left(1 + 3(-\ln|\epsilon|)^{2/3}C^{-2/3}\right)^2. \tag{31}$$

The number of plane waves is illustrated in Fig. 7 as a function of the near-field parameter C for three error levels. One can observe that the convergence rate is high since the number of plane waves varies slowly with respect to ϵ. One can also note that the powers of the near-field coefficient C and of $-\ln|\epsilon|$ present in (31) are equal to those obtained in [15] and [29] in the context of the error control of the FMM algorithm.

TABLE I
NUMBER OF PLANE-WAVE P FOR THREE ERROR LEVELS $|\epsilon|$ AND DISTANCES z

$\lvert\epsilon\rvert$	10^{-2}	10^{-3}	10^{-4}
z/z_f	1.5	5	15
$C/\ln\lvert\epsilon\rvert$	0.11	0.023	0.0057
P	27	27	47

Next, we establish a relation between the number of plane waves (31) and the DoF of the scattered field [15], defined as the minimum number of orthonormal basis functions needed to represent a given field distribution. Let us consider two spheres of minimum radius ρ_s and ρ_o enclosing source and observation domains for which centers $\mathbf{r}_o$ and $\mathbf{r}_s$ are separated by a distance $z = ||\mathbf{r}_s - \mathbf{r}_o||$, respectively. By setting the relative error $|\epsilon|$ to one and ρ to $\rho_s + \rho_o$ in (31) in order to account for the sizes of both the source and the observation domains, we obtain

$$P_0 = \frac{k^2(\rho_o + \rho_s)^4}{4\pi z^2}. \tag{32}$$

When the observation domain is a disk, the number of DoF $N_0 = (k\rho_s\rho_o/z)^2/\pi$ is obtained by taking the square of (30) in [15] and multiplying it with $\pi/4$. From there, we can write

$$\frac{P_0}{N_0} = \frac{(\rho_o + \rho_s)^4}{4\rho_s^2\rho_o^2} \tag{33}$$

for which a minimum value $P_0/N_0 = 4$ is achieved for $\rho_o = \rho_s$. When the observation domain is reduced to a point, i.e., $\rho_o = 0$, N_0 goes to zero while P_0 does not. The differences between N_0 and P_0 could be explained by noting that we are specifically targeting an IPW representation. For instance, we can mention that the *a priori* extraction of a phase factor $e^{-jk||\mathbf{r}-\mathbf{r}_s||}$ of the field over the observation domain, considered in the approach of [14] and [15], has not been performed in this paper.

Finally, for increasing far-field distances, i.e., when $C/\ln|\epsilon| \to 0$, it can be easily proven from (15), (21), and (25) that the number of plane waves converges toward

$$P = \frac{(-\ln|\epsilon|)^2}{\pi} \tag{34}$$

which only depends on the target accuracy $|\epsilon|$. This minimum number is higher than one and mathematically translates the intuition that interferences between plane waves are necessary to produce the $1/r$-decay of far fields. Table I illustrates the number of plane waves P, obtained by solving the Gauss quadrature [31], for three error levels $|\epsilon|$. The distances z are expressed in terms of the Fraunhoffer limit z_f defined in (10) and are selected subject to the relative error of the far-field approximation extracted from Fig. 1 in [32] is equal to $|\epsilon|$.

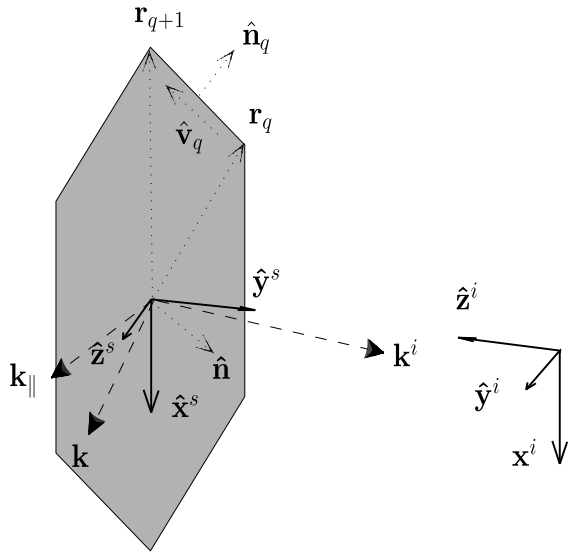

Fig. 8. Vectorial quantities and local CS.

One can infer that the number of plane waves increases with $|\epsilon|$ according to (34) and remains large at far-field distances. However, in contrast to the far-field approximation, the IPW decomposition can achieve arbitrary error levels for a given distance z.

V. Numerical Results

The sampling rules derived in Sections III and IV are applied to the near-to-intermediate field evaluation of the PO radiation integral. For planar structures, e.g., walls in urban scattering, the PWS of the scattered field can be directly expressed in terms of the incident one since the spatial integral (6) is analytical [24], [25]. Hence, the integrals are carried out in the spectral domain and the calculation does not require any spatial mesh.

A. Spectral-Domain Physical Optics

Let us consider an incident field represented by a sum of P_i plane waves

$$\mathbf{E}^i(\mathbf{r}) = \sum_m^{P^i} \mathbf{E}^i_m e^{-j\mathbf{k}^i_m \cdot \mathbf{r}} \tag{35}$$

where $\mathbf{E}^i_m$ and $\mathbf{k}^i_m$ are expressed in a local CS "s" $(\hat{\mathbf{x}}^s, \hat{\mathbf{y}}^s, \hat{\mathbf{z}}^s)$ centered on the scatterer and oriented toward the observation domain, as illustrated in Fig. 8.

In PO theory, the current density on a perfectly electrical conductor (PEC) object is directly expressed from the tangential component of the incident magnetic field as $\mathbf{J} = 2\hat{\mathbf{n}} \times \mathbf{H}^i = 2\hat{\mathbf{n}} \times (\mathbf{k}^i \times \mathbf{E}^i)/(k\eta)$ with $\hat{\mathbf{n}}$ the unit normal to the surface. By substituting (35) into (7), we express the PWS of the current as

$$\tilde{\mathbf{J}}(\mathbf{k}) = \tfrac{2}{k\eta} \textstyle\sum_m \left(\hat{\mathbf{n}} \times (\mathbf{k}^i_m \times \mathbf{E}^i_m)\right) W(\mathbf{k} - \mathbf{k}^i_m). \tag{36}$$

The window function W corresponds to the Fourier transform of a complex exponential over a polygonal domain

$$W(\mathbf{k}) = \iint e^{j\mathbf{k}\cdot\mathbf{r}} dS'. \tag{37}$$

When the surface S' is planar, the integral has an analytical primitive thanks to Green's theorem. This is derived in Appendix H and may be viewed as an extension of results from [26] to complex wavenumbers. The result reads

$$W(\mathbf{k}) = \frac{1}{jk_\parallel^2} \sum_{q=1}^{Q} L_q (\mathbf{k} \cdot \hat{\mathbf{n}}_q) \operatorname{sinc}\left(\mathbf{k} \cdot \hat{\mathbf{v}}_q \frac{L_q}{2}\right) e^{j\mathbf{k}\cdot(\mathbf{r}_q + L_q \hat{\mathbf{v}}_q/2)} \tag{38}$$

where Q is the number of corners of a polygonal scatterer, $\mathbf{r}_q$ is the position vector of the qth corner, $\hat{\mathbf{v}}_q = (\mathbf{r}_{q+1} - \mathbf{r}_q)/L_q$ is the unit segment direction with $L_q = ||\mathbf{r}_{q+1} - \mathbf{r}_q||$, $\hat{\mathbf{n}}_q = \hat{\mathbf{v}}_q \times \hat{\mathbf{n}}$ is the in-plane outgoing unit normal to the segment, $\mathbf{k}_\parallel = \mathbf{k} - (\hat{\mathbf{n}} \cdot \mathbf{k})\hat{\mathbf{n}}$ is the component of the wave-vector parallel to the surface with $k_\parallel^2 = \mathbf{k}_\parallel \cdot \mathbf{k}_\parallel$. Those geometrical quantities are illustrated in Fig. 8.

Finally, the scattered electrical field $\mathbf{E}^s$ is evaluated within the observation domain through (4). The computational cost of the method is directly related to the computation of the nested sums when we substitute (36) into (4). If P^i and P^s are the number of plane waves required for the incident and the scattered spectrum, the computational complexity for evaluating the required IPW spectral samples of the scattered field is $\mathcal{O}(P^i P^s)$.

B. Examples

Let us suppose an incident field produced by a vertically polarized Hertzian dipole located at $\mathbf{r}^i$ that impinges on a PEC square plate of length L. We will evaluate the total field, defined as $\mathbf{E} = \mathbf{E}^i + \mathbf{E}^s$, within an observation domain that lies on a second virtual square plate. This example may be viewed as a subproblem of an urban propagation scenario, with PO evaluation of double-scattering by walls. A comparison is carried out between the spectral method and a spatial-domain integration using a Simpson rule and N sample points. The relative error is numerically evaluated with

$$\epsilon(\mathbf{r}) = \sqrt{\frac{(\mathbf{E}(\mathbf{r}) - \mathbf{E}^d(\mathbf{r})) \cdot (\mathbf{E}(\mathbf{r}) - \mathbf{E}^d(\mathbf{r}))^*}{\mathbf{E}(\mathbf{r}) \cdot \mathbf{E}(\mathbf{r})^\star}} \tag{39}$$

where (*) stands for complex conjugate. According to definition (6), the field PWS of a dipole is analytically given by

$$\tilde{\mathbf{E}}^{il}(\mathbf{k}^{il}) = -jk\eta(\hat{\mathbf{p}}^l - (\mathbf{k}^{il} \cdot \hat{\mathbf{p}}^l)\mathbf{k}^{il}/k^2) \tag{40}$$

where $\hat{\mathbf{p}}^l$ is the polarization of the dipole and superscript l means that the quantities are expressed in a local CS "i" with $(\hat{\mathbf{x}}^i, \hat{\mathbf{y}}^i, \hat{\mathbf{z}}^i)$ centered on the dipole and oriented toward the center of the scatterer, as illustrated in Fig. 8. In contrast, vectors defined in (35) were expressed in the CS "s." Hence, we will use a rotation matrix $\mathbf{R}$, as provided in Appendix G, in order to transform vectors expressed in CS "i" into vectors expressed in CS "s." This transformation reads as

$$\mathbf{E}^i_m = w^{il}_m \mathbf{R} \cdot \tilde{\mathbf{E}}^{il}(\mathbf{k}^{il}_m) e^{-j\mathbf{k}^i_m \cdot \mathbf{r}^i} \tag{41}$$

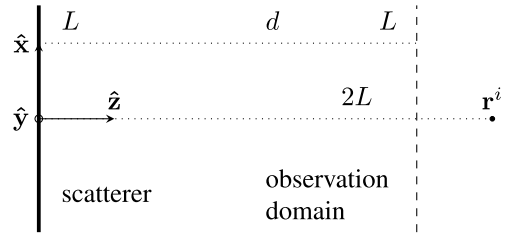

Fig. 9. Scattering scenario 1. A vertical dipole (dotted) illuminates a square plate (solid). Observation domain lies on a second plate (dashed) separated by a distance d.

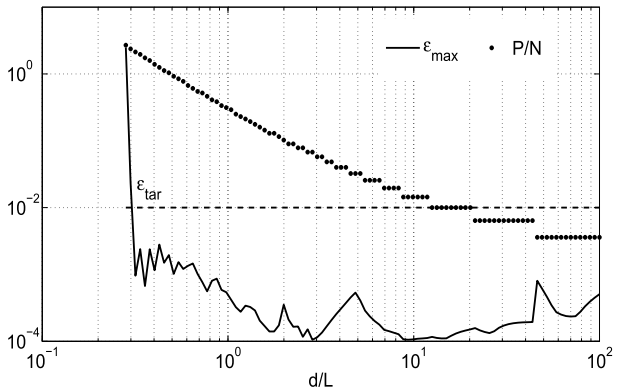

Fig. 10. Maximum relative error $\epsilon_{\max}$ (solid), target relative error ϵ_{tar} (dashed), and ratio P/N of number of plane waves to number of spatial samples (dotted).

where $\mathbf{k}_m^i = \mathbf{R} \cdot \mathbf{k}_m^{il}$, $w_m^{il} = -j(1+ja)^2 \Delta k^2/(8\pi^2 k_{z,m}^{il})$ and the indices (p, q) in (4) and (5) have been concatenated into a single index m.

1) Varying the Relative Distance: In this example, we consider two parallel plates of length $L = 10\ \lambda$ separated by a distance d and a point source located at a distance $2L$ from the scatterer, as illustrated in Fig. 9. A target error level of $\epsilon_{\text{tar}} = 10^{-2}$ has been chosen. The PWS of the incident and the scattered field is evaluated with the help of (15), (21), and (30) in which the triplet $(\rho, z, |\epsilon|)$ is replaced by $(\sqrt{2}L/2, 2L, \epsilon_{\text{tar}})$ and $(\sqrt{2}L, d, \epsilon_{\text{tar}})$, respectively. The resulting number of plane waves in the IPW decomposition of the incident field is $P^i \approx 200$. The far-field results correspond to a ratio $d \geq z_f/L = 40$ m. In Fig. 10, we have plotted the maximum value of the relative error $\epsilon_{\max} = \max_{\mathbf{r}} \epsilon(\mathbf{r})$ over the observation domain for a varying distance d. As expected, one can observe that $\epsilon_{\max}$ (solid line) is below ϵ_{tar} (dashed line) for distances d satisfying conditions (16). More precisely, the error is controlled down to $d \approx 0.3L$. This contributes to validating the paraxial approximation (8) used to derive the sampling rules in this paper. It is worth recalling that the paraxial approximation is not made when estimating the PWS. A spatial sampling step of $\lambda/10$ has been empirically chosen for the numerical integration in the spatial domain subject to the corresponding discretization error is much smaller than ϵ_{tar}. This leads to $N = 10^4$ spatial samples. In order to provide a theoretical measure of the acceleration ratio of the spectral method, the ratio P/N is also plotted in Fig. 10. A comparison between the computation times of the spatial domain and the spectral-domain methods is shown in Fig. 11.

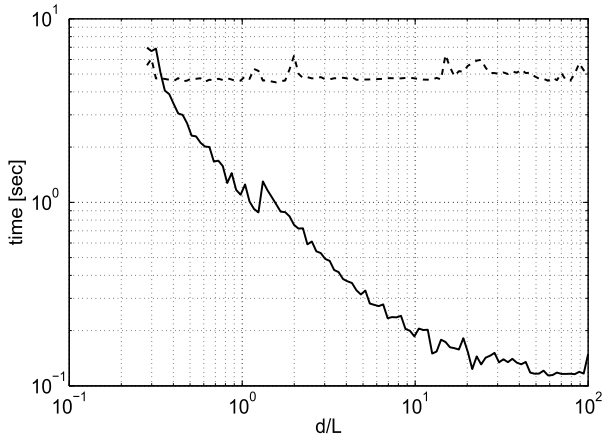

Fig. 11. Computation times (in seconds) of the spatial-domain integration (dashed) and of the spectral-domain method (solid).

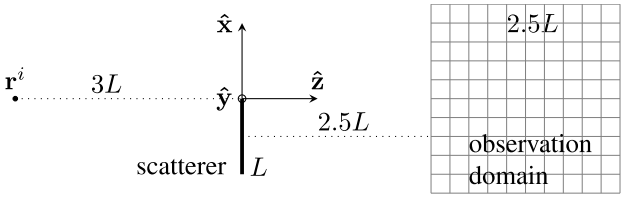

Fig. 12. Scattering scenario 2. A vertical dipole (dotted) illuminates a square plate (solid). Observation domain lies on a horizontal second plate (grid).

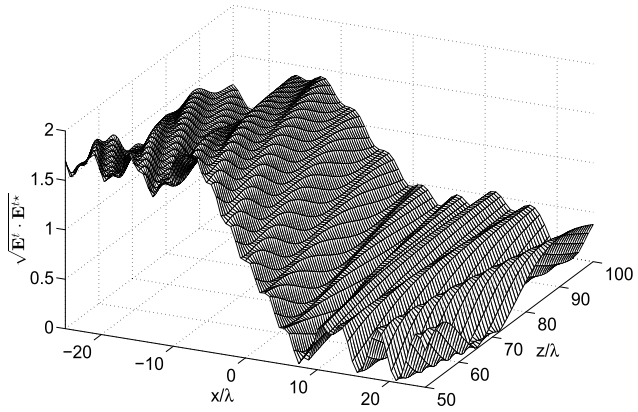

Fig. 13. Magnitude of the total electrical field in configuration shown in Fig. 12.

The simulations are carried out using a PC with 16-GB RAM and Processor Intel (R) Core(TM) i5-3570 CPU at 3.4 GHz. One can infer that the speed-up factor becomes important, i.e., one to two orders of magnitude, when the field of view $L/(2d)$ is reduced.

2) Forward Scattering: The geometry of the scenario is sketched in Fig. 12. The dipole is now located at a distance $3L$ from a plate of length $L = 20\ \lambda$. The amplitude of the total field is computed within a horizontal square plate of length $L = 2.5\ L$ contained in the plane $y = 0$ and located at a distance $d = 2.5\ \lambda$ from the scatterer. A target error of $\epsilon_{\text{tar}} = 10^{-3}$ has been selected. This example may be found critical since the observation domain crosses the shadow boundary. The magnitude of the total electrical field and the relative error are illustrated in Figs. 13 and 14, respectively. As expected, one observes that the magnitude

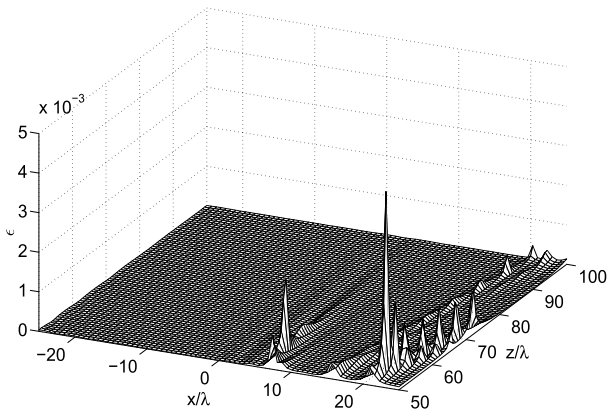

Fig. 14. Relative error of the IPW decomposition of the total electrical field for $\epsilon_{\text{tar}} = 10^{-3}$ in configuration shown in Fig. 12.

of the field reaches low values in Fig. 13 which correspond to peak values of ϵ in Fig. 14. For this scenario, we infer that the relative error of Green's function is not representative of the relative error of the total field since it does not take into account the possible destructive interference between the incident and the scattered field. Nevertheless, one can note that those higher values remain of the order of ϵ_{tar} in Fig. 14. The PWS of the incident field is sampled with $a = 0.63$, $k_{mr} = 0.3\ k$, $\Delta k = 0.03\ k$ and $P^i = 240$. The PWS of the scattered field is sampled with $a = 0.3$, $k_{mr} = 0.95\ k$, $\Delta k = 0.02\ k$ and $P = 7300$. The number of spatial samples is $N = 10^4$. Hence, the speed-up factor is less important for this example since the field of view is still large.

VI. Conclusion

We proposed an integration scheme and sampling rules for the field IPW decomposition based on a linear contour for given error level ϵ. This expansion is well suited to scattering problems in which interacting groups are visible from each other within a limited angular sector. We derived concise expressions for the contour slope, the truncation limit, and the sampling step which are accurate when the field of view ρ/z is smaller than one and the distance z is larger than the wavelength. It has been demonstrated that the required number of plane waves follows a similar dependence with respect to $k\rho$, kz, and ϵ as the number of DoF of the scattered field defined in [15]. The integration scheme has been applied to the evaluation of the PO radiation integral in the intermediate-to-far field. By expressing directly the scattered PWS in terms of the incident one, the computations can be entirely performed in the spectral domain. We are, thus, able to avoid any spatial sampling and associated discretization errors. The corresponding computational cost becomes proportional to the product of the DoF of the incident and the scattered field.

Generally, the subsequent methodology can be followed for an IPW decomposition.

1) A local CS is defined with its z-axis oriented from the center of the source domain toward the center of the observation domain.
2) The relative distance z between the two domains is evaluated and the maximum radial extend ρ of both domains are summed up.
3) The contour slope, the truncation limit, and the sampling are selected with

$$a = \left(1 - \frac{C}{\ln|\epsilon|}\right)^{-1/3}$$

$$k_{mr} = \frac{k\rho}{z}\left(\frac{1}{2} + \sqrt{\frac{1}{4} - \frac{\ln|\epsilon|}{aC}}\right)$$

$$\Delta k = \frac{2\pi}{(1+a^2)\rho}\left(\frac{1}{2} + \sqrt{\frac{1}{4} - \frac{\ln|\epsilon|}{aC}}\right)^{-1}$$

   where $C = k\rho^2/z$ is the near-field parameter and ϵ is the targeted relative error.
4) The field PWS is numerically computed with (36) for PO current on a polygonal scatterer and with (6) for an arbitrary source distribution.
5) The electric field is evaluated on the observation domain using (4).

The provided sampling rules could also be used to accelerate the evaluation of intermediate fields, from a few wavelengths to a few times the Fraunhoffer distance, in fast method-of-moments implementations based on IPWs, such as FIPWA [1] or HIPWA [22], or in the context of the spectral theory of diffraction [33].

Appendix A
Truncation Error

With (1), (9), and (8), the truncation error is given by

$$\epsilon = \frac{-jz}{k} e^{jk\rho^2/(2z)} \int_{k_m}^{\infty} e^{jk_\rho^2 z/(2k)} J_0(k_m\rho) k_\rho \mathrm{d}k_\rho. \quad (42)$$

Performing a first-order integration by parts leads to

$$\epsilon = -e^{jk\rho^2/(2z) + jk_\rho^2 z/(2k)} J_0(k_\rho\rho) - R \quad (43)$$

for which the remainder is

$$R = \rho e^{jk\rho^2/(2z)} \int_{k_m}^{\infty} e^{jk_\rho^2 z/(2k)} J_1(k_\rho\rho) \mathrm{d}k_\rho. \quad (44)$$

Let us consider a flat contour with $k_{\rho i} = k_{mi}$. Using the Cauchy–Schwarz inequality and an upper bound on the amplitude of the Bessel function $|J_1(x)| < e^{|x_i|}$, we can write

$$|R| \leq \rho e^{k_{mi}\rho} \int_{k_{mr}}^{\infty} e^{-k_{mi}k_{\rho r}z/k} \mathrm{d}k_{\rho r} \quad (45)$$

for which the integral is analytical

$$|R| \leq \frac{k\rho}{k_{mi}z} e^{-k_{mr}k_{mi}z/k + k_{mi}\rho}. \quad (46)$$

Anticipating the relation $k_{mr} \sim k\rho/z$ from (15), we have

$$|\epsilon| \leq e^{-k_{mr}k_{mi}z/k + k_{mi}\rho}\,(1 + \mathcal{O}(k_{mr}/k_{mi})). \quad (47)$$

APPENDIX B
DISCRETIZATION ERROR

The series (18) converges fast enough to keep only the strongest replica of indices (m, n). When $|\Delta y| \ll z$, we can use (9) to obtain

$$\epsilon \approx e^{jk(\rho^2-(x-m\Delta x)^2-(y-n\Delta y)^2)/(2z)} \tag{48}$$

where $\Delta y = \Delta x = 2\pi/((1 + ja)\Delta k)$ and the magnitude is

$$|\epsilon| = e^{(mx-Dm^2+ny-Dn^2)ka\,D/z} \tag{49}$$

with $D = 2\pi/((1 + a^2)\Delta k)$. For a conical field of view of radius ρ, the maximum error is achieved when $(m, n) = \{(1, 0); (0, 1)\}$ and $(x, y) = \{(\rho, 0); (0, \rho)\}$ and is given by

$$-\ln|\epsilon| \approx (D - \rho)\, ka\, D/z. \tag{50}$$

APPENDIX C
ERROR OF THE DYADIC GREEN'S FUNCTION

The element ij of the absolute error $\bar{\mathbf{e}}^a$ of the IPW decomposition of the dyadic Green's function $\bar{\mathbf{G}}^d$ is given by

$$\bar{e}^a_{ij} = \bar{G}_{ij} - \bar{G}^d_{ij} = e^a + \frac{1}{k^2}\frac{\partial^2 e^a}{\partial u_i \partial u_j} \tag{51}$$

where $(u_1, u_2, u_3) \equiv (x, y, z)$. $e^a = G - G^d$ is the absolute error of the IPW decomposition of the scalar Green's function G^d which can be decomposed as $e^a = e^a_t + e^a_d$ where

$$\begin{aligned} e^a_t &\approx -\frac{e^{-jkz}}{4\pi z} e^{jk^2_m z/(2k)} J_0(k_m\rho) \\ e^a_d &\approx \frac{e^{-jkz}}{4\pi z} e^{-jk(x-m\Delta x)^2/(2z)-jk(y-n\Delta y)^2/(2z)}. \end{aligned} \tag{52}$$

In (52), e^a_t refers to absolute errors resulting from truncation (Appendix A) while e^a_d refers to absolute errors resulting from discretization (Appendix B). Considering only a e^{-jkz} dependence with respect to z yields $\partial e^a/\partial z \approx -jke^a$. For $i = (1, 2)$ and $m = n = 1$, the partial derivatives are expressed as

$$\frac{\partial e^a}{\partial u_i} = \frac{-jk}{z}(u_i - \Delta x)e^a_d - jk_m\frac{u_i}{\rho}\frac{J_1(k_m\rho)}{J_0(k_m\rho)}e^a_t \tag{53}$$

where division by J_0 has been introduced to let e^a_t appear in the numerator. Using the results $k_m \sim k\rho/z$ obtained in (15) and $\Delta x \sim \rho$ from (21) leads to $\partial e^a/\partial u_i \sim k\rho/z e^a$.

We can now compare the second term of (51) with the first term. Deriving with respect to u_1, u_2 multiplies the error level by $k\rho/z$. Hence, e^a is multiplied by $\rho^2/z^2 \ll 1$ given observation in limited fields of view. Thus, the first term of (51) dominates. Since that term is simply proportional to the scalar Green's function, the error analysis of the latter is sufficient to analyze the error of the vector field in the already defined field of view.

APPENDIX D
ROUND-OFF ERROR

In practice, each spectral variable in the integrand of (2) is rounded by the computer. However, we have experimentally observed that the round-off of k_z in the exponential has a stronger impact for $z \gg \lambda$. Assuming a simple multiplicative noise $1+n(k_{xr}, k_{yr})$, we can perform a first-order Taylor series expansion of this exponential and use $k_z \approx k$ to obtain

$$e^{-jk_z z(1+n)} \approx (1 - jnkz)e^{-jk_z z}. \tag{54}$$

With the help of (8) and (9), the relative round-off error can be written as

$$\begin{aligned} \epsilon \approx \frac{-jz^2}{2\pi} e^{jk\rho^2/(2z)} \iint n e^{jk^2_\rho z/(2k)} \\ \times e^{-jk_x x - jk_y y}\frac{k_\rho}{k_{\rho r}}\frac{\mathrm{d}k_\rho}{\mathrm{d}k_{\rho r}}\mathrm{d}k_{xr}\mathrm{d}k_{yr}. \end{aligned} \tag{55}$$

Using the Cauchy–Schwarz inequality and $|n| \le 2\epsilon_m$ within (55), the round-off error for a linear contour is bounded by

$$|\epsilon| \le \frac{-j\epsilon_m z^2}{\pi}(1 + a^2)\iint e^{a(-k^2_\rho z/k + k_{xr}x + k_{yr}y)}\mathrm{d}k_{xr}\mathrm{d}k_{yr} \tag{56}$$

where a is the straight contour slope and ϵ_m is the double-precision machine error level. Finally, we have

$$|\epsilon| \le kz\epsilon_m\frac{1 + a^2}{a}e^{ak\rho^2/(4z)}. \tag{57}$$

APPENDIX E
OPTIMAL INTEGRATION SCHEME

Dividing the truncation limit of (15) by the sampling step of (21) leads to

$$\frac{k_m}{\Delta k} = \frac{C}{4\pi}(1 + a^2)\left(1 - \frac{2\ln|\epsilon|}{aC} + \sqrt{1 - \frac{4\ln|\epsilon|}{aC}}\right). \tag{58}$$

Performing a first-order Taylor approximation of the square root yields

$$\sqrt{\pi P} \sim \frac{C}{2}(1 + a^2)\left(1 - \frac{2\ln|\epsilon|}{aC}\right) \tag{59}$$

where P is given in (25). When the approximation (28) is accurate, i.e., $-C/\ln|\epsilon| \gg 1$, we can write

$$\sqrt{\pi P} \sim \frac{C}{2} + \frac{3C^{1/3}}{2}(-\ln|\epsilon|)^{2/3} + C^{-1/3}(-\ln|\epsilon|)^{4/3}. \tag{60}$$

Finally, by dropping the last term, we obtain

$$P \sim \frac{C^2}{4\pi}\left(1 + 3(-\ln|\epsilon|)^{2/3}C^{-2/3}\right)^2. \tag{61}$$

APPENDIX F
OPTIMAL CONTOUR SLOPE

Equalizing the derivative of (26) to zero and defining $e = -C/\ln|\epsilon|$ leads to

$$ea^3 + a^2 - 1 = 0. \tag{62}$$

If $\zeta = (27e^2 - 2 + ((27e^2 - 2)^2 - 4)^{1/2})/2$, the real positive root is given by

$$a = -\frac{1}{3e} + \frac{\zeta^{1/3}}{3e} + \frac{\zeta^{-1/3}}{3e}. \tag{63}$$

APPENDIX G
ROTATION MATRIX

Let us first define the local CS "i" $(\hat{\mathbf{x}}^i, \hat{\mathbf{y}}^i, \hat{\mathbf{z}}^i)$ and "s" $(\hat{\mathbf{x}}^s, \hat{\mathbf{y}}^s, \hat{\mathbf{z}}^s)$, in which the IPW decomposition of the incident field and the scattered field are performed, the center positions of a source domain $\mathbf{r}^{so}$, a scatterer $\mathbf{r}^{sc}$, and an observation domain $\mathbf{r}^o$. All those vectors are expressed in a global CS $(\hat{\mathbf{x}}, \hat{\mathbf{y}}, \hat{\mathbf{z}})$. The local CS "i" and "s" have their z-axis pointing from $\mathbf{r}^{so}$ to $\mathbf{r}^{sc}$ and from $\mathbf{r}^{sc}$ to $\mathbf{r}^o$, respectively. Thus, we have $\hat{\mathbf{z}}^i = \mathbf{r}^{sc} - \mathbf{r}^{so}/||\mathbf{r}^{sc} - \mathbf{r}^{so}||$ and $\hat{\mathbf{z}}^s = \mathbf{r}^o - \mathbf{r}^{sc}/||\mathbf{r}^o - \mathbf{r}^{sc}||$. Then, considering two arbitrary vectors $\mathbf{v}^i$ and $\mathbf{v}^s$, which are, respectively, not parallel to $\hat{\mathbf{z}}^i$ and $\hat{\mathbf{z}}^s$, we have $\hat{\mathbf{x}}^i = \hat{\mathbf{z}}^i \times \mathbf{v}^i/||\hat{\mathbf{z}}^i \times \mathbf{v}^i||$ and $\hat{\mathbf{x}}^s = \hat{\mathbf{z}}^s \times \mathbf{v}^s/||\hat{\mathbf{z}}^s \times \mathbf{v}^s||$. The rotation matrices that transform vectors expressed in a local CS to vectors in the global CS are

$$\mathbf{R}^{s,i} = \begin{pmatrix} \hat{\mathbf{x}}^{s,i} \\ \hat{\mathbf{y}}^{s,i} \\ \hat{\mathbf{z}}^{s,i} \end{pmatrix}. \tag{64}$$

Finally, the rotation matrix for passing from a local CS "i" to a local CS "s" is

$$\mathbf{R} = \mathbf{R}^{s^T}\mathbf{R}^i \tag{65}$$

where the superscript T means transposition.

APPENDIX H
FOURIER TRANSFORM OVER A POLYGONAL DOMAIN

We are looking for an analytical expression for the Fourier transform of an exponential over a polygonal domain

$$W(\mathbf{k}) = \iint e^{j\mathbf{k}\cdot\mathbf{r}} dS'. \tag{66}$$

In order to reduce the surface integral to a line integral, we will use the divergence theorem. Hence, we need to find a vectorial function $\mathbf{f}$ subject to $\nabla_s \cdot \mathbf{f} = \nabla \cdot (\mathbf{f} - (\hat{\mathbf{n}} \cdot \mathbf{f})\hat{\mathbf{n}}) = e^{j\mathbf{k}\cdot\mathbf{r}}$ where $\nabla\cdot$ is the divergence operator and $\hat{\mathbf{n}}$ is the outgoing normal to the surface. A function satisfying this property is

$$\mathbf{f} = \frac{\mathbf{k}_\parallel}{jk_\parallel^2} e^{j\mathbf{k}\cdot\mathbf{r}} \tag{67}$$

where $\mathbf{k}_\parallel = \mathbf{k} - (\hat{\mathbf{n}} \cdot \mathbf{k})\hat{\mathbf{n}}$ is the component of the wave-vector parallel to the surface and $k_\parallel^2 = \mathbf{k}_\parallel \cdot \mathbf{k}_\parallel$. Using the surface divergence theorem, we can rewrite it as a line integral over the boundary of the polygon

$$W(\mathbf{k}) = \frac{1}{jk_\parallel^2} \int \mathbf{k}_\parallel \cdot \hat{\mathbf{n}}_o e^{j\mathbf{k}\cdot\mathbf{r}} d\Gamma \tag{68}$$

where Γ is the boundary of the planar domain and $\mathbf{n}_o$ is the unit outgoing normal to the segment. Since we are considering a polygonal shaped surface, we can integrate over each boundary segment separately, which yields

$$W(\mathbf{k}) = \frac{1}{jk_\parallel^2} \sum_{q=1}^{Q} L_q (\mathbf{k} \cdot \hat{\mathbf{n}}_q) \operatorname{sinc}\left(\mathbf{k} \cdot \hat{\mathbf{v}}_q \frac{L_q}{2}\right) e^{j\mathbf{k}\cdot(\mathbf{r}_q + L_q \hat{\mathbf{v}}_q/2)} \tag{69}$$

where Q is the number of corners, $\mathbf{r}_q$ is the position vector of the qth corner, $\hat{\mathbf{v}}_q = (\mathbf{r}_{q+1} - \mathbf{r}_q)/L_q$ is the unit segment direction with $L_q = ||\mathbf{r}_{q+1} - \mathbf{r}_q||$, $\hat{\mathbf{n}}_q = \hat{\mathbf{v}}_q \times \hat{\mathbf{n}}$ is the in-plane outgoing unit normal to the segment. Those quantities are illustrated in Fig. 8.

ACKNOWLEDGMENT

The authors would like to thank the reviewers for their constructive comments.

REFERENCES

[1] B. Hu, W. C. Chew, and S. Velamparambil, "Fast inhomogeneous plane wave algorithm for the analysis of electromagnetic scattering," *Radio Sci.*, vol. 36, no. 6, pp. 1327–1340, Nov./Dec. 2001.

[2] L. J. Jiang and W. C. Chew, "Low-frequency fast inhomogeneous plane-wave algorithm (LF-FIPWA)," *Microw. Opt. Technol. Lett.*, vol. 40, no. 2, pp. 117–122, Jan. 2004.

[3] K. Alkhalifeh, G. Hislop, N. A. Ozdemir, and C. Craeye, "Efficient MoM simulation of 3-D antennas in the vicinity of the ground," *IEEE Trans. Antennas Propag.*, vol. 64, no. 12, pp. 5335–5344, Dec. 2016.

[4] B. Hu and W. C. Chew, "Fast inhomogeneous plane wave algorithm for scattering from objects above the multilayered medium," *IEEE Trans. Geosci. Remote Sens.*, vol. 39, no. 5, pp. 1028–1038, May 2001.

[5] M. Di Vico, F. Frezza, L. Pajewski, and G. Schettini, "Scattering by buried dielectric cylindrical structures," *Radio Sci.*, vol. 40, p. RS6S18, Dec. 2005.

[6] Q. Gueuning, C. Craeye, and C. Oestges, "Inhomogeneous plane-wave spectrum based physical optics," in *Proc. Int. Conf. Electromagn. Adv. Appl. (ICEAA)*, Turin, Italy, Sep. 2015, pp. 1460–1463.

[7] R. Coifman, V. Rokhlin, and S. Wandzura, "The fast multipole method for the wave equation: A pedestrian prescription," *IEEE Antennas Propag. Mag.*, vol. 35, no. 3, pp. 7–12, Jun. 1993.

[8] J. E. Hansen, J. Hald, F. Jensen, and F. H. Larsen, *Spherical Near-Field Antenna Measurements*. London, U.K.: Peregrinus, 1988.

[9] D. Slepian, "Prolate spheroidal wave functions, Fourier analysis and uncertainty—IV: Extensions to many dimensions; generalized prolate spheroidal functions," *Bell Syst. Tech. J.*, vol. 43, no. 6, pp. 3009–3057, Nov. 1964.

[10] O. M. Bucci, C. Gennarelli, and C. Savarese, "Optimal interpolation of radiated fields over a sphere," *IEEE Trans. Antennas Propag.*, vol. 39, no. 11, pp. 1633–1643, Nov. 1991.

[11] K. Tap, "Complex source point beam expansions for some electromagnetic radiation and scattering problems," Ph.D. dissertation, Dept. Elect. Comput. Eng., Ohio State Univ., Columbus, OH, USA, 2007.

[12] J. M. Arnold, "Phase-space localization and discrete representations of wave fields," *J. Opt. Soc. Amer. A, Opt. Image Sci.*, vol. 12, no. 1, pp. 111–123, Jan. 1995.

[13] E. Michielssen and W. C. Chew, "Fast steepest descent path algorithm for analyzing scattering from two-dimensional objects," *Radio Sci.*, vol. 31, no. 5, pp. 1215–1224, Sep./Oct. 1996.

[14] O. M. Bucci and G. Franceschetti, "On the spatial bandwidth of scattered fields," *IEEE Trans. Antennas Propag.*, vol. AP-35, no. 12, pp. 1445–1455, Dec. 1987.

[15] O. M. Bucci and G. Franceschetti, "On the degrees of freedom of scattered fields," *IEEE Trans. Antennas Propag.*, vol. 37, no. 7, pp. 918–926, Jul. 1989.

[16] J. A. Kong, Ed., *Theory of Electromagnetic Waves*. Hoboken, NJ, USA: Wiley, 1975.

[17] S. Ohnuki and W. C. Chew, " Error analysis of the fast inhomogeneous plane-wave algorithm for 2D free-space cases," *Microw. Opt. Technol. Lett.*, vol. 38, no. 4, pp. 300–304, Aug. 2003.

[18] D. M. Pozar, "Input impedance and mutual coupling of rectangular microstrip antennas," *IEEE Trans. Antennas Propag.*, vol. AP-30, no. 6, pp. 1191–1196, Nov. 1982.

[19] K. A. Michalski and J. R. Mosig, "Multilayered media green's functions in integral equation formulations," *IEEE Trans. Antennas Propag.*, vol. 45, no. 3, pp. 508–519, Mar. 1997.

[20] R. Borghi, F. Frezza, C. Santini, and G. Schettini, and M. Santarsiero, "Numerical study of the reflection of cylindrical waves of arbitrary order by a generic planar interface," *J. Electromagn. Waves Appl.*, vol. 13, no. 1, pp. 27–50, Jan. 1999.

[21] S. N. Jha and C. Craeye, "Contour-FFT based spectral domain MBF analysis of large printed antenna arrays," *IEEE Trans. Antennas Propag.*, vol. 62, no. 11, pp. 5752–5764, Nov. 2014.

[22] E. Martini, C. Craeye, N. Ozdemir, and S. Maci, "Harmonics-based inhomogeneous plane-wave method (HIPW)," *IEEE Trans. Antennas Propag.*, vol. 63, no. 5, pp. 2331–2336, May 2015.
[23] E. Martini, S. Karki, C. Craeye and, and S. Maci, "Error analysis of the harmonics-based plane wave method," in *Proc. Int. Conf. Electromagn. Adv. Appl. (ICEAA)*, Turin, Italy, Sep. 2015, pp. 1493–1495.
[24] W. Gordon, "Far-field approximations to the Kirchoff-Helmholtz representations of scattered fields," *IEEE Trans. Antennas Propag.*, vol. AP-23, no. 4, pp. 590–592, Jul. 1975.
[25] S.-W. Lee and R. Mittra, "Fourier transform of a polygonal shape function and its application in electromagnetics," *IEEE Trans. Antennas Propag.*, vol. AP-31, no. 1, pp. 99–103, Jan. 1983.
[26] P. L. Garcia-Muller and A. G. Roederer, "A physical optics based plane wave spectrum approach to the analysis of finite planar antennas," *IEEE Trans. Antennas Propag.*, vol. 40, no. 8, pp. 906–911, Aug. 1992.
[27] W. C. Chew, *Waves and Fields in Inhomogenous Media*. New York, NY, USA: Van Nostrand Reinhold, 1990.
[28] C. Craeye, "A series representation for the intermediate-field transmittance between apertures," in *Proc. URSI Int. Symp. Electromagn. Theory*, Espoo, Finland, Aug. 2016, pp. 240–242.
[29] W. C. Chew, J.-M. Jin, E. Michielssen, and J. Song, Eds., *Fast and Efficient Algorithms in Computational Electromagnetics*. Norwood, MA, USA: Artech House, 2001.
[30] J. A. Stratton, *Electromagnetic Theory*. New York, NY, USA: McGraw-Hill, 1941.
[31] Wikipedia.org. *Gauss Circle Problem*. Accessed: Dec. 22, 2018. [Online]. Available: https://en.wikipedia.org/wiki/Gauss
[32] S. Jiang-Sheng and G. Ben-Qing, "Critical distance of far field for basic radiation element," in *Proc. Int. Symp. Electromagn. Compat.*, Qingdao, China, Oct. 2007, pp. 375–377.
[33] R. Mittra, Y. Rahmat-Samii, and W. L. Ko, "Spectral theory of diffraction," *Appl. Phys.*, vol. 10, no. 1, pp. 1–13, 1976.

Quentin Gueuning received the B.Sc. and M.Sc. degrees from the Université catholique de Louvain, Louvain-la-Neuve, Belgium, in 2012 and 2014, respectively, where he is currently pursuing the Ph.D. degree with the Institute of Information and Communication Technologies, Electronics and Applied Mathematics (ICTEAM).

Since 2014, he has been a Research Assistant with ICTEAM, Université catholique de Louvain. His current research interests include fast computational methods, high-frequency theories, and radio-channel characterization.

Christophe Craeye (M'98–SM'11) was born in Ronse, Belgium, in 1971. He received the degree in electrical engineering in 1994, the B.Phil. degree, and the Ph.D. degree in applied sciences from the Université catholique de Louvain (UCLouvain), Louvain-la-Neuve, Belgium, in 1994 and 1998, respectively.

From 1994 to 1999, he was a Teaching Assistant with UCLouvain, where he carried out research on the radar signature of the sea surface perturbed by rain, in collaboration with NASA and ESA. From 1999 to 2001, he was a Post-Doctoral Researcher with the Eindhoven University of Technology, Eindhoven, The Netherlands. He was with the University of Massachusetts, Amherst, MA, USA, in 1999. He was with the Netherlands Institute for Research in Astronomy, Dwingeloo, The Netherlands, in 2001. In 2002, he started an antenna research activity with UCLouvain. He was with the Astrophysics and Detectors Group, University of Cambridge, Cambridge, U.K., in 2011. He is currently a Professor with UCLouvain. His research was funded by the Region Wallonne, European Commission, ESA, FNRS, and UCL. His current research interests include mutual coupling, finite antenna arrays, wideband antennas, small antennas, metamaterials, fast physical optics and numerical methods for fields in periodic media, with applications to communication and sensing systems.

Dr. Craeye was a recipient of the 2005–2008 Georges Vanderlinden Prize from the Belgian Royal Academy of Sciences in 2009. He was an Associate Editor of the IEEE TRANSACTIONS ON ANTENNAS AND PROPAGATION from 2004 to 2010 and the IEEE ANTENNAS AND WIRELESS PROPAGATION LETTERS from 2011 to 2017.

Claude Oestges (M'05–SM'12–F'16) received the M.Sc. and Ph.D. degrees in electrical engineering from the Université catholique de Louvain (UCLouvain), Louvain-la-Neuve, Belgium, in 1996 and 2000, respectively.

In 2001, he joined the Smart Antennas Research Group (Information Systems Laboratory), Stanford University, Stanford, CA, USA, as a Post-Doctoral Scholar. From 2002 to 2005, he was a Post-Doctoral Fellow of the Belgian Fonds de la Recherche Scientifique (FRS-FNRS) with the Microwave Laboratory UCLouvain. He is currently a Full Professor with the Electrical Engineering Department, Institute for Information and Communication Technologies, Electronics and Applied Mathematics, UCLouvain. He has authored or co-authored three books and more than 200 journal papers and conference communications.

Dr. Oestges is the Chair of COST Action CA15104 IRACON from 2016 to 2020. He was a recipient of the 1999–2000 IET Marconi Premium Award and of the IEEE Vehicular Technology Society Neal Shepherd Award in 2004 and 2012.